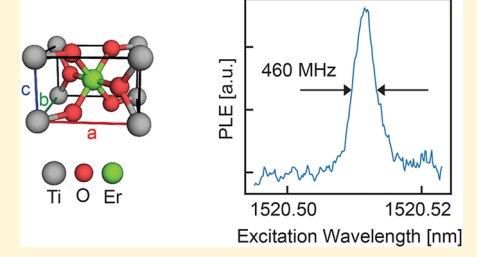
Downloaded via UNIV OF CHICAGO on October 4, 2020 at 20:48:34 (UTC). See https://pubs.acs.org/sharingguidelines for options on how to legitimately share published articles.

Narrow Optical Line Widths in Erbium Implanted in TiO₂

Christopher M. Phenicie, †,§ Paul Stevenson, †,§ Sacha Welinski, †,§ Brendon C. Rose, † Abraham T. Asfaw, † Robert J. Cava, Stephen A. Lyon, Nathalie P. de Leon, and Jeff D. Thompson*,

Supporting Information

ABSTRACT: Atomic and atomlike defects in the solid state are widely explored for quantum computers, networks, and sensors. Rare earth ions are an attractive class of atomic defects that feature narrow spin and optical transitions that are isolated from the host crystal, allowing incorporation into a wide range of materials. However, the realization of long electronic spin coherence times is hampered by magnetic noise from abundant nuclear spins in the most widely studied host crystals. Here, we demonstrate that Er3+ ions can be introduced via ion implantation into TiO2, a host crystal that has not been studied extensively for rare earth ions and has a low natural abundance of nuclear spins. We observe efficient incorporation of the implanted Er3+ into the Ti4+ site (>50% yield) and



measure narrow inhomogeneous spin and optical line widths (20 and 460 MHz, respectively) that are comparable to bulkdoped crystalline hosts for Er3+. This work demonstrates that ion implantation is a viable path to studying rare earth ions in new hosts and is a significant step toward realizing individually addressed rare earth ions with long spin coherence times for quantum technologies.

KEYWORDS: Rare earth ions, ion implantation, erbium, optical spectroscopy, electron spin resonance, quantum optics

Rare earth ion impurities in crystalline hosts are a promising platform for quantum technologies, combining narrow, stable optical transitions with isolated electronic or nuclear spins. Crystals doped with ensembles of rare earth ions (REIs) have been used to demonstrate a variety of quantum memory protocols for quantum networks, demonstrating coherence times of hours, light-matter entanglement, and quantum state teleportation. Fecent work has focused on individually addressed REIs⁵⁻⁷ and has made significant steps toward spin-photon entanglement with single ions, including the demonstration of radiatively broadened optical transitions and single-shot spin readout^{9,10} in optical nanocavities. Other efforts have focused on quantum transduction from microwave to optical frequencies. ^{11–13} Among several widely studied REIs, erbium is particularly well suited to many of these tasks, as its telecom-wavelength optical transition enables low-loss propagation in optical fibers and integration with silicon nanophotonics. 14

There are several materials challenges to future development of REI-based quantum technologies. First, abundant nuclear spins in the host crystal limit REI electronic spin coherence times, despite work on several mitigation strategies including using clock states in hyperfine isotopes 15,16 or electronic states with small magnetic moments.¹⁷ The vast majority of studied hosts for REIs involve at least one element with no stable spin-0 nuclear isotopes, including all yttrium-based hosts [e.g., Y₂SiO₅ (YSO), Y₃Al₅O₁₂ (YAG), YLiF₄ and Y₂O₃], as well as alkali halides and lithium niobate (a notable exception is CaWO₄¹⁸). Second, it is difficult to isolate single REIs in the well-studied yttrium-based materials because they are typically

contaminated with ppm-level concentrations of all rare earth elements. 19,14 Finally, the incorporation of REIs into crystalline hosts typically involves bulk doping during growth, which precludes controllable positioning and the isolation of individual defects.

Ion implantation is an established route to controllably introducing small numbers of defects into a wide range of host materials, and in the context of quantum emitters, it has found recent application in creating isolated color centers in diamond. 20-23 However, ion implantation has not been extensively studied in the context of REIs in crystalline hosts, particularly in the low-density regime. Ion-implanted $\rm Er^{3+}:YSO^{24}$ and $\rm Gd^{3+}:Al_2O_3^{25}$ have been studied in electron spin resonance (ESR), and ion-implanted Ce³⁺:YAG^{26,27} and Pr³⁺:YAG²⁸ have been studied in single-center confocal microscopy. In these works, increased line widths were observed compared to those of bulk-doped crystals, presumably as a result of unrepaired lattice damage resulting from ion implantation. In contrast, localized Er3+ doping in LiNbO3 using solid diffusion has yielded bulklike properties.²⁹

In this work, we study the properties of implanted Er3+ in single-crystal rutile TiO2. On the basis of its elemental composition, this host material is largely free of trace REI impurities and has a low abundance of nuclear spins (Ti: 87% I = 0; O: 99.96% I = 0), which could be reduced further using

Received: September 16, 2019 Revised: November 11, 2019 Published: November 25, 2019

[†]Department of Electrical Engineering and [‡]Department of Chemistry, Princeton University, Princeton, New Jersey 08544, United States

isotopically enriched Ti precursors. Bulk-doped Er³⁺:TiO₂ (rutile) has previously been observed in electron spin resonance (ESR) in the context of maser development, 30,31 and Er3+ in anatase TiO2 has been studied in photoluminescence (PL).³² Here, we use ESR and PL spectroscopy to demonstrate that implanted Er3+ ions in TiO2 have inhomogeneous spin and optical line widths (20 and 460 MHz, respectively) that are comparable to or smaller than typical values for bulk-doped Er³⁺ in most host crystals.³³ The Er3+ ions that we observe occupy substitutional Ti4+ sites with D_{2h} symmetry, and we hypothesize that the narrow line widths are a consequence of the nonpolar symmetry of this site. We determine the energy of the lowest few ground- and excitedstate crystal field levels. For the sample processing conditions that lead to the highest yield, we find that >50% of the implanted Er3+ ions are situated in Ti4+ sites.

Samples of rutile TiO_2 (MTI) with (001) orientation were implanted with erbium ions with a range of energies of up to 350 keV chosen to achieve a uniform Er^{3+} concentration in the first 100 nm of the crystal and total fluences of 9×10^{11} cm⁻² (hereafter, low dose) and 9×10^{13} cm⁻² (high dose). After implantation, some samples were annealed in air at temperatures of up to 800 °C (Table 1 and ref 34). We look for

Table 1. List of Samples Used in This Work

no.	total fluence	annealing conditions	implantation yield	data shown in figure
1	$9 \times 10^{13} \text{ cm}^{-2}$	as implanted	$3 \pm 1\%$	3a,b, 4b
2	9×10^{13}	270 °C, 2 h in air	7 ± 3%	1c
3	9×10^{13}	340 °C, 2 h in air	14 ± 6%	1a, 2b-d, 3c, 4b
4	9×10^{13}	800 °C, 1 h in air	94 ± 38%	4b,c
5	$9 \times 10^{11} \text{ cm}^{-2}$	as implanted	$54 \pm 22\%$	
6	9×10^{11}	270 °C, 2 h in air	46 ± 18%	
7	9×10^{11}	340 °C, 2 h in air	$55 \pm 22\%$	1b
8	9 × 10 ¹¹	800 °C, 1 h in air	67 ± 27%	4c

evidence of implanted erbium using photoluminescence excitation (PLE) spectroscopy in a helium cryostat, performed by scanning a chopped laser and collecting delayed fluorescence onto a low-noise photodiode. The resulting spectrum (Figure 1a) shows several sharp absorption resonances near 1.5 μ m, with the narrowest having a total line width of 460 MHz (Figure 1b). During the scan, we measure the fluorescence lifetime at each excitation wavelength (Figure 1c) and find that the four starred peaks have the same lifetime (5.25 \pm 0.03 ms) and some of the smaller peaks have a shorter lifetime (2.51 \pm 0.04 ms).

In the site symmetries possible in rutile space group $P4_2/mnm$, the ground $(^4I_{15/2})$ and excited $(^4I_{13/2})$ electronic states of Er^{3+} split into eight and seven Kramers' doublets labeled Z_{1-8} and Y_{1-7} , respectively (Figure 2a). Absorption lines arise from transitions from $Z_1 \rightarrow Y_m$, and fluorescence occurs primarily from $Y_1 \rightarrow Z_m$ regardless of which Y level is excited, because of rapid nonradiative relaxation to Y_1 . 19,35 We conjecture that the four starred peaks in Figure 1a correspond to transitions from $Z_1 \rightarrow Y_1 - Y_4$ in the same Er^{3+} site. To check this hypothesis, we filter the fluorescence through a grating spectrometer to resolve the emission wavelength in a PL

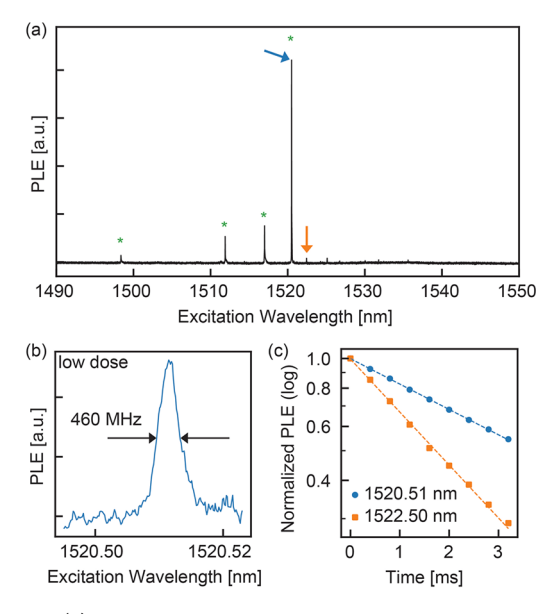


Figure 1. (a) PLE spectrum at 11 K in a high-dose sample. Stars indicate lines belonging to $Z_1 \rightarrow Y_1 - Y_4$ transitions of the same $\mathrm{Er^{3+}}$ site, as determined by PL (Figure 2). (b) Spectrum at 5 K of the $Z_1 - Y_1$ transition in a low-dose sample, demonstrating the narrowest observed inhomogeneous line width of 460 MHz (fwhm). (c) Fluorescence lifetime measurements under excitation at the wavelengths indicated by arrows in (a). The long (blue dots) lifetime is 5.25 ± 0.03 ms, and the short (orange squares) lifetime is 2.51 ± 0.04 ms. The other starred peaks in (a) exhibit the same lifetime as the blue curve.

measurement (Figure 2b) while exciting at each of these peaks. The emission spectra are qualitatively similar, with a principal peak at 1520 nm and a series of smaller peaks at longer wavelengths, confirming this hypothesis. Furthermore, the absence of any shorter-wavelength emission confirms that 1520 nm is the $Z_1 \rightarrow Y_1$ transition.

The emission spectrum also allows several of the Z energy levels to be determined. These measurements are performed at $T=11\,$ K to increase the excitation efficiency by homogeneously broadening the optical transition, but at these temperatures, several excited Y states are appreciably thermally populated and contribute extra lines to the emission spectrum. These transitions can be separated using temperature-dependent PL spectroscopy (Figure 2c), where lines with the same temperature dependence are interpreted to originate from the same Y_i level (Figure 2d). This allows us to assign energies to the first five ground states $Z_1 - Z_5$ and confirms the first three Y assignments determined from Figure 1a. We additionally note that the PL line intensities show that the dominant decay pathways for the first few excited states are Y_1 to Z_1 , Y_2 to Z_2 , and Y_3 to Z_3 and Z_4 .

Next, we probe the spin properties of the Z_1 doublet using ESR in an X-band continuous wave (CW) spectrometer. We identify the Er³+ peak through its characteristic high g factor ($g_{zz}=14.37\pm0.04$) and hyperfine spectrum ($^{167}{\rm Er}^{3+}$ with I=7/2 and 23% abundance, $A_{zz}=1503\pm11$ MHz, Figure 3a). The magnetic moment varies strongly with the magnetic field orientation, with its maximal value along the [001] direction (c axis). The effective g factor in the [100] direction is 1.41 ± 0.31 , as determined from a fit to the orientation dependence in both the data in Figure 3b and a measurement with the crystal in another orientation, which allowed for measurement of the full g tensor. 34 We note that these g factors are not consistent

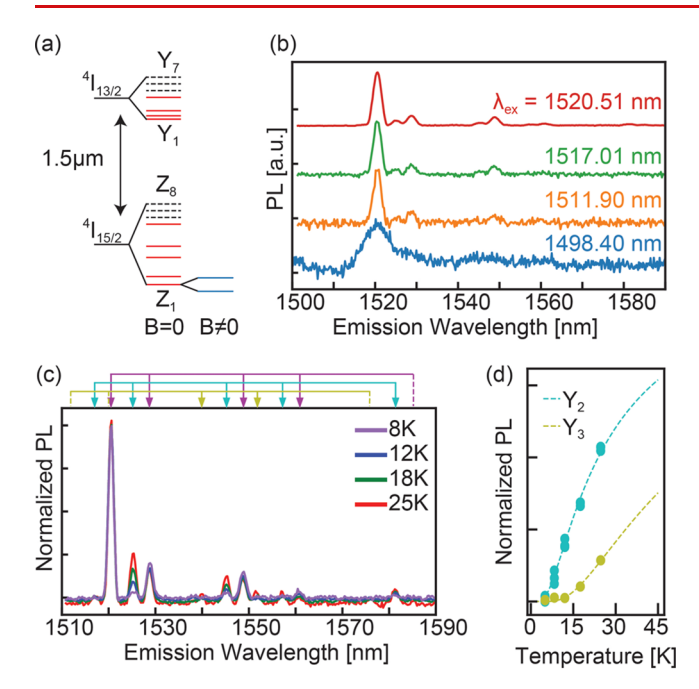


Figure 2. (a) Level structure of Er3+:TiO2. Solid red lines indicate crystal field levels in the ${}^4I_{15/2}$ and ${}^4I_{13/2}$ manifolds measured in this work (also listed in Table 2). Unobserved levels are depicted with dashed lines. Each line is a Kramers' doublet, which splits into two sublevels when a magnetic field is applied. (b) Emission spectrum observed when exciting on the $Z_1 \rightarrow Y_1 - Y_4$ transitions at the indicated wavelength λ_{ex} . The line widths are instrument-limited, with a wider slit width for the 1498.40 nm measurement because the fluorescence was very weak. (c) Emission spectrum with $Z_1 \rightarrow Y_1$ excitation at several temperatures, normalized to the $Y_1 \rightarrow Z_1$ peak. The magenta, cyan, and yellow arrows indicate groupings of lines corresponding to decay to Z_1 – Z_5 from Y_1 , Y_2 , and Y_3 , respectively. Lines without arrowheads are not observed. (d) Temperature dependence of the PL intensity for different lines in (c). Dashed lines (cyan and yellow, corresponding to arrows of the same color in (c)) are the expected PL intensities as a function of temperature assuming thermal equilibrium within the Y manifold.

Table 2. Energy Levels for Er³⁺:TiO₂^a

			energy	
term	level	THz	nm (vac.)	cm^{-1}
$^{4}I_{15/2}$	Z_1	0		0
	Z_2	1.06		35.3
	Z_3	3.61		120
	Z_4	5.10		170
	Z_5	8.05		268
	$Z_6 - Z_8$		not observed	
$^{4}I_{13/2}$	Y_1	197.1651	1520.515	6576.719
	Y_2	197.6204	1517.012	6591.905
	Y_3	198.2888	1511.898	6614.203
	Y_4	200.0745	1498.404	6673.767
	$Y_5 - Y_7$		not observed	

^aThe uncertainty in the Y energies is 200 MHz, determined from a wavemeter calibrated to an acetylene absorption cell. The uncertainty in the Z levels is \sim 10 GHz, based on fits to the data in Figure 2b.

with those previously reported for Er^{3+} : TiO_2 ($g_{zz}=15.1, g_{xxy}g_{yy}<0.1$), 30 although the hyperfine constant is similar to the previously reported value ($A=1484~\mathrm{MHz}$).

To probe whether the Er³⁺ site identified in ESR is the same as the one in the optical measurements above, we illuminate

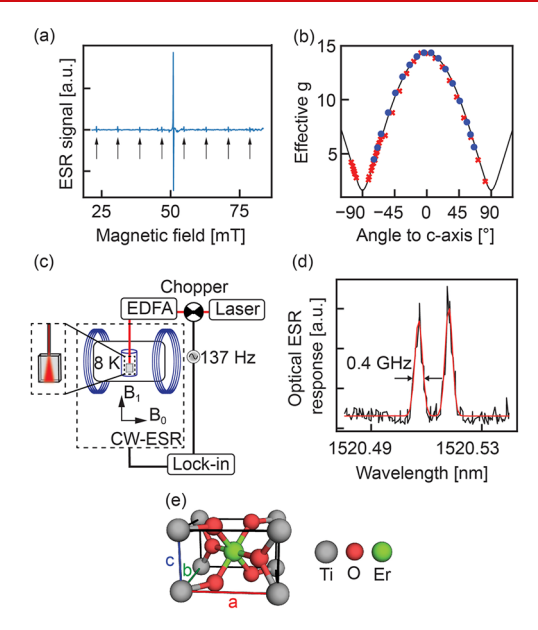


Figure 3. (a) CW ESR spectrum with the magnetic field nearly parallel to the c axis of the crystal. Arrows point to hyperfine lines in the spectrum belonging to the $^{167}\mathrm{Er^{3+}}$ ions. (b) Angular variation of the effective g factor of $\mathrm{Er^{3+}}$ in the ac (red crosses) and bc (blue circles) planes. (c) Schematic of the optical-ESR setup. The sample sits in a CW ESR spectrometer and is illuminated by a laser delivered through an optical fiber. When the laser is resonant with the $Z_1 \rightarrow Y_1$ optical transition, we observe a change in the ESR signal from population shelving in the excited state. To increase sensitivity, we measure this optical ESR response by chopping the excitation light and measuring the modulated ESR signal via lock-in detection. (d) The optical ESR response is resonant at the same wavelength as the $Z_1 - Y_1$ spectral line in Figure 1, indicating that the spin and optical transitions arise from the same $\mathrm{Er^{3+}}$ site. (e) Unit cell of $\mathrm{TiO_2}$ (rutile). We propose that $\mathrm{Er^{3+}}$ occupies a $\mathrm{Ti^{4+}}$ site, as shown in green.

the sample with light near the $Z_1 \rightarrow Y_1$ line and observe the resulting change in the ESR signal. The experimental apparatus for this measurement is depicted in Figure 3c. The ESR signal changes when the laser is resonant with the $Z_1 \rightarrow Y_1$ optical transition (Figure 3d) because some fraction of the Er³⁺ ions are transferred to the Y_1 state and are no longer resonant with the microwaves. This confirms that the optical and ESR measurements probe the same Er³⁺ site. In a magnetic field, the $Z_1 \rightarrow Y_1$ transition splits into four lines. Here, only two are observed, presumably because the other two are weak or orthogonal to the light polarization direction. From the splitting, we can extract the Y_1 magnetic moment along the caxis, g_{zz}^e : the spacing between the peaks corresponds to a difference in g factors $|g_{zz}^g - g_{zz}^e| = 2.105 \pm 0.013$, implying $g_{zz}^e =$ $12.19 \pm 0.04 < g_{zz}^g$ since the larger value is larger than the maximum possible value of 14.4 for ${}^4I_{13/2}$.

The rotational dependence of g is essentially identical in the ac and bc crystallographic planes; however, we observe that the single line splits into two lines when the field is rotated slightly into the ab plane³⁴. These observations suggest that Er^{3+} is incorporated into a well-defined crystallographic site with two orientations differing by a 90 deg rotation around the c-axis, which is consistent with substitutional incorporation on the Ti^{4+} site with D_{2h} symmetry. This incorporation site has been suggested based on similar measurement techniques for a range of transition metal impurities in TiO_2 , including iron,³⁶ manganese³⁷ and others;³⁰ in contrast, nickel is incorporated

into an interstitial site and gives a qualitatively different ESR spectrum.³⁸

Finally, we study the dependence of the ion properties on implantation and annealing conditions. First, the implantation yield in the Ti⁴⁺ site (measured using quantitative ESR³⁴) depends strongly on the implantation dose (Figure 4a).

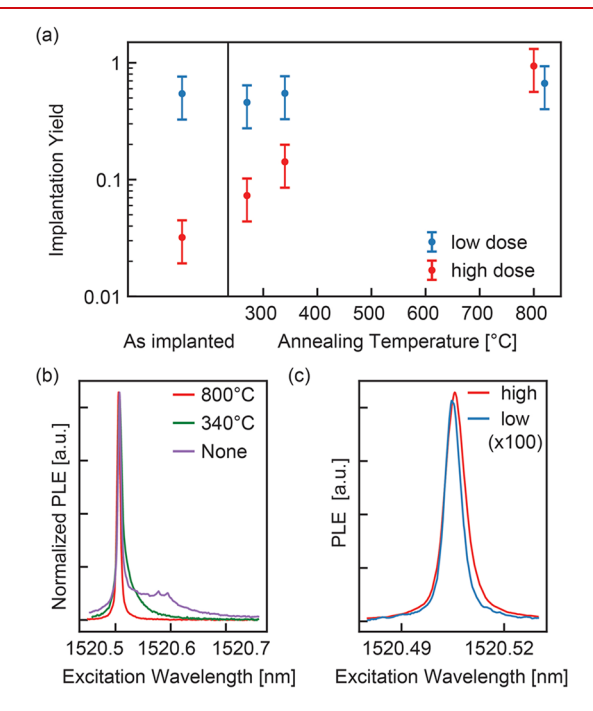


Figure 4. (a) Implantation yield, measured using quantitative ESR, as a function of implantation and annealing conditions. The error bars primarily reflect systematic uncertainty in the reference sample, and the two points at 800 °C are horizontally offset by a small amount for clarity. (b) PLE spectrum at $T=10~{\rm K}$ of the $Z_1 \rightarrow Y_1$ transition in the high-dose sample after different annealing conditions, demonstrating the reduction of the inhomogneous line width as implantation damage is repaired. (c) PLE spectrum at $T=10~{\rm K}$ of the $Z_1 \rightarrow Y_1$ transition in the low-dose and high-dose samples after an 800 °C anneal, showing line widths of 670 \pm 10 and 840 \pm 10 MHz, respectively. The low-dose data is scaled by the ratio of the implantation doses, demonstrating that the implantation yield after annealing is similar.

Without postimplantation annealing, the yield for low-dose implantation is $54 \pm 22\%$, but for high-dose implantation it is only $3 \pm 1\%$. After annealing in air for 1 h at 800 °C, the yield for the high-dose sample increases to 94 ± 38 and $67 \pm 27\%$ in the low-dose sample. The optical lineshapes also change with implantation and annealing conditions. Figure 4b shows the PLE spectrum of the $Z_1 \rightarrow Y_1$ transition in the high-dose sample as a function of annealing temperature, demonstrating a significant reduction in the overall peak width. Figure 4c shows the PLE spectrum of the $Z_1 \rightarrow Y_1$ transition in the low-dose and high-dose samples after 800 °C annealing, demonstrating that after annealing both samples achieve narrow linewidths. In contrast, the inhomogeneous spin line width 34 does not change with dose or annealing conditions.

We now turn to a discussion of these results. Several important properties follow from the symmetry of the D_{2h} incorporation site. First, the optical transition should be a nearly purely magnetic dipole (MD) in nature since the inversion-symmetric crystal field cannot mix 4f and 5d states to introduce a forced electric dipole transition. The observed

excited-state lifetime of 5.25 ms is consistent with the predicted MD decay rate of 5–6.7 ms,³⁹ depending on the TiO_2 refractive index for the polarization direction of the dipole ($n_o = 2.45$, $n_e = 2.70$).⁴⁰ Second, an expected consequence of the nonpolar nature of this site is that the wave functions should not have a permanent electric dipole moment, eliminating first-order sensitivity of the optical transitions to electric fields. We hypothesize that the observed narrow inhomogeneous line widths are partially a consequence of this insensitivity. In future work, it will be interesting to probe whether the lack of a permanent dipole moment leads to long coherence of the optical transitions.

Previous studies of ion implantation in ${\rm TiO_2}$ using Rutherford backscattering have reported nearly unity substitutional fractions of Sn and Hf implanted in ${\rm TiO_2}$ at fluences of up to $3\times 10^{15}~{\rm cm^{-2}}$ without significant lattice damage and that significant lattice damage from implanting La (which does not substitute ${\rm Ti^{4+}}$) can be reversed by annealing above 900 °C. ⁴¹ The Er³⁺ properties that we measure under different implantation and annealing conditions are consistent with a picture that lattice damage caused by ion implantation adversely affects the defect properties, and the amount of damage is proportional to the implantation dose and can be reduced by postimplantation thermal annealing. The dependence of the implantation yield on dose is similar to reported values for ${\rm Ce^{3+}}$ and ${\rm Pr^{3+}}$ in YAG. ^{27,28}

An important question about the incorporation of trivalent Er³⁺ into the Ti⁴⁺ site is how charge compensation is achieved. In many materials, including alkali halides and CaF2, local charge compensation in nearest- or next-nearest-neighbor sites around aliovalent defects is observed through a lowering of the symmetry and an increase in the number of spectral lines, 42 while in other materials, such as CaWO₄, 43 SrTiO₃, 44 and TiO₂₁³⁰ this effect is weak or absent and the charge compensation is believed to be long-range. Since our ESR spectra are consistent with a single crystallographic site with two orientations, we conclude that the charge compensation is remote for Er³⁺:TiO₂. On the basis of a broad ESR scan, we believe that our sample has non-negligible concentrations of several transition-metal impurities, and changes in their valence state may also play a role, along with oxygen vacancies. We cannot rule out that a small minority of Er3+ sites have a local charge-compensating defect.

We conclude with a discussion of prospects for building quantum systems out of individually addressed Er3+ ions in TiO₂ using nanophotonic circuits. The apparent strong branching ratio of Y_1 to Z_1 is favorable for Purcell enhancement of the emission, and we note that MD Purcell enhancement can be of a similar magnitude to the more common electric dipole enhancement. 14 Furthermore, the low implantation dose used here is already quite high from the perspective of single ion studies, corresponding to an areal density of $10^4 \mu m^{-2}$ and an average defect spacing of 21 nm, suggesting that high implantation yield and narrow linewidths can be expected in the relevant density range for single-ion work. The significant reduction in the concentration of nuclear magnetic moments compared to that of typical Er³⁺ hosts such as YSO and YAG may enable extended electronic spin coherence times and open the door to manipulating individual nuclear spins, 45 and further reduction of the nuclear magnetism may be accomplished by the CVD growth 46 of isotopically enriched layers.

We note that these results, together with recent work on implanted color centers in diamond, ^{23,22,21} suggest that good defect properties can be achieved using ion implantation and thermal annealing. In contrast to doping during growth, ion implantation allows the rapid exploration of many materials and defects. This approach may be extended to search for other hosts for rare earth ions as well as other optically active defects, which may be attractive for a wide range of quantum technologies including computing, communications, and sensing.

ASSOCIATED CONTENT

Supporting Information

The Supporting Information is available free of charge at https://pubs.acs.org/doi/10.1021/acs.nanolett.9b03831.

Additional measurements of the *g* tensor, further details of implantation and annealing conditions, and a description of the quantitative ESR measurement (PDF)

AUTHOR INFORMATION

Corresponding Author

*E-mail: jdthompson@princeton.edu.

ORCID ®

Jeff D. Thompson: 0000-0001-8673-052X

Author Contributions

§These authors contributed equally to this work

Notes

The authors declare no competing financial interest.

ACKNOWLEDGMENTS

We gratefully acknowledge helpful conversations with Philippe Goldner, early technical contributions to the apparatus from Henry Ando and Zheru Qiu, and assistance with data collection from Sabrina Chern. Funding for this research was provided by the AFOSR (contract FA9550-18-1-0334), the Eric and Wendy Schmidt Transformative Technology Fund, the Princeton Catalysis Initiative, and the Princeton Center for Complex Materials (PCCM), an NSF-funded MRSEC (DMR-1420541). We acknowledge the use of Princeton's Imaging and Analysis Center, which is partially supported by PCCM, as well as the Princeton Micro-Nano Fabrication Lab. C.M.P is supported by an NDSEG graduate fellowship.

■ REFERENCES

- (1) Tittel, W.; Afzelius, M.; Chaneliére, T.; Cone, R.; Kröll, S.; Moiseev, S.; Sellars, M. Laser Photonics Rev. 2010, 4, 244–267.
- (2) Zhong, M.; Hedges, M. P.; Ahlefeldt, R. L.; Bartholomew, J. G.; Beavan, S. E.; Wittig, S. M.; Longdell, J. J.; Sellars, M. J. *Nature* **2015**, *517*, 177–180.
- (3) Clausen, C.; Usmani, I.; Bussiéres, F.; Sangouard, N.; Afzelius, M.; De Riedmatten, H.; Gisin, N. *Nature* **2011**, 469, 508–512.
- (4) Bussières, F.; Clausen, C.; Tiranov, A.; Korzh, B.; Verma, V. B.; Nam, S. W.; Marsili, F.; Ferrier, A.; Goldner, P.; Herrmann, H.; Silberhorn, C.; Sohler, W.; Afzelius, M.; Gisin, N. *Nat. Photonics* **2014**, *8*, 775–778.
- (5) Kolesov, R.; Xia, K.; Reuter, R.; Stöhr, R.; Zappe, A.; Meijer, J.; Hemmer, P.; Wrachtrup, J. Nat. Commun. 2012, 3, 1029.
- (6) Nakamura, I.; Yoshihiro, T.; Inagawa, H.; Fujiyoshi, S.; Matsushita, M. Sci. Rep. 2015, 4, 7364.
- (7) Eichhammer, E.; Utikal, T.; Götzinger, S.; Sandoghdar, V. New J. Phys. 2015, 17, 083018.

(8) Zhong, T.; Kindem, J. M.; Bartholomew, J. G.; Rochman, J.; Craiciu, I.; Verma, V.; Nam, S. W.; Marsili, F.; Shaw, M. D.; Beyer, A. D.; Faraon, A. *Phys. Rev. Lett.* **2018**, *121*, 183603.

- (9) Raha, M.; Chen, S.; Phenicie, C. M.; Ourari, S.; Dibos, A. M.; Thompson, J. D. *eprint arXiv:1907.09992* **2019**, 1–19.
- (10) Kindem, J. M.; Ruskuc, A.; Bartholomew, J. G.; Rochman, J.; Huan, Y. Q.; Faraon, A. *eprint arXiv:1907.12161* **2019**, 1–36.
- (11) Williamson, L. A.; Chen, Y. H.; Longdell, J. J. Phys. Rev. Lett. 2014, 113, 203601.
- (12) O'Brien, C.; Lauk, N.; Blum, S.; Morigi, G.; Fleischhauer, M. *Phys. Rev. Lett.* **2014**, *113*, 063603.
- (13) Fernandez-Gonzalvo, X.; Chen, Y.-H.; Yin, C.; Rogge, S.; Longdell, J. J. Phys. Rev. A: At., Mol., Opt. Phys. 2015, 92, 062313.
- (14) Dibos, A. M.; Raha, M.; Phenicie, C. M.; Thompson, J. D. Phys. Rev. Lett. 2018, 120, 243601.
- (15) McAuslan, D. L.; Bartholomew, J. G.; Sellars, M. J.; Longdell, J. J. Phys. Rev. A: At., Mol., Opt. Phys. 2012, 85, 032339.
- (16) Ortu, A.; Tiranov, A.; Welinski, S.; Fröwis, F.; Gisin, N.; Ferrier, A.; Goldner, P.; Afzelius, M. Nat. Mater. 2018, 17, 671–675.
- (17) Lim, H. J.; Welinski, S.; Ferrier, A.; Goldner, P.; Morton, J. J. Phys. Rev. B: Condens. Matter Mater. Phys. 2018, 97, 064409.
- (18) Rakhmatullin, R. M.; Kurkin, I. N.; Mamin, G. V.; Orlinskii, S. B.; Gafurov, M. R.; Baibekov, E. I.; Malkin, B. Z.; Gambarelli, S.; Bertaina, S.; Barbara, B. *Phys. Rev. B: Condens. Matter Mater. Phys.* **2009**, *79*, 172408.
- (19) Liu, G.; Jacquier, B. Spectroscopic Properties of Rare Earths in Optical Materials; Springer-Verlag: Berlin, 2005.
- (20) Toyli, D. M.; Weis, C. D.; Fuchs, G. D.; Schenkel, T.; Awschalom, D. D. Nano Lett. **2010**, 10, 3168-3172.
- (21) Chu, Y.; et al. Nano Lett. 2014, 14, 1982-1986.
- (22) Rose, B. C.; Huang, D.; Zhang, Z.-H.; Stevenson, P.; Tyryshkin, A. M.; Sangtawesin, S.; Srinivasan, S.; Loudin, L.; Markham, M. L.; Edmonds, A. M.; Twitchen, D. J.; Lyon, S. A.; de Leon, N. P. *Science* **2018**, *361*, 60–63.
- (23) Sipahigil, A.; et al. Science 2016, 354, 847-850.
- (24) Probst, S.; Kukharchyk, N.; Rotzinger, H.; Tkalčec, A.; Wünsch, S.; Wieck, A. D.; Siegel, M.; Ustinov, A. V.; Bushev, P. A. *Appl. Phys. Lett.* **2014**, *105*, 162404.
- (25) Wisby, I. S.; De Graaf, S. E.; Gwilliam, R.; Adamyan, A.; Kubatkin, S. E.; Meeson, P. J.; Tzalenchuk, A. Y.; Lindström, T. *Phys. Rev. Appl.* **2016**, *6*, 024021.
- (26) Xia, K.; Kolesov, R.; Wang, Y.; Siyushev, P.; Reuter, R.; Kornher, T.; Kukharchyk, N.; Wieck, A. D.; Villa, B.; Yang, S.; Wrachtrup, J. *Phys. Rev. Lett.* **2015**, *115*, 093602.
- (27) Kornher, T.; Xia, K.; Kolesov, R.; Kukharchyk, N.; Reuter, R.; Siyushev, P.; Stöhr, R.; Schreck, M.; Becker, H. W.; Villa, B.; Wieck, A. D.; Wrachtrup, J. Appl. Phys. Lett. 2016, 108, 053108.
- (28) Groot-Berning, K.; Kornher, T.; Jacob, G.; Stopp, F.; Dawkins, S. T.; Kolesov, R.; Wrachtrup, J.; Singer, K.; Schmidt-Kaler, F. *Phys. Rev. Lett.* **2019**, *123*, 106802.
- (29) Thiel, C. W.; Sun, Y.; Macfarlane, R. M.; Böttger, T.; Cone, R. L. J. Phys. B: At., Mol. Opt. Phys. **2012**, 45, 124013.
- (30) Gerritsen, H. J. Paramagnetic Resonance of Transition Metal Ions in Rutile (TiO₂). In *Paramagnetic Resonance: Proceedings of the First International Conference*; Jerusalem, Israel, 1962; Low, W., Ed.; Academic Press, 1963; pp 3–12.
- (31) Sabisky, E. S.; Gerritsen, H. J. Doubly doped titanium dioxide maser element. U.S. Patent 3 275 558, Sept 27, 1966.
- (32) Luo, W.; Fu, C.; Li, R.; Liu, Y.; Zhu, H.; Chen, X. Small 2011, 7, 3046–3056.
- (33) Thiel, C.; Böttger, T.; Cone, R. J. Lumin. 2011, 131, 353-361.
- (34) See the Supporting Information.
- (35) Böttger, T.; Sun, Y.; Thiel, C. W.; Cone, R. L. Phys. Rev. B: Condens. Matter Mater. Phys. **2006**, 74, 075107.
- (36) Carter, D. L.; Okaya, A. Phys. Rev. 1960, 118, 1485-1490.
- (37) Gerritsen, H. J.; Sabisky, E. S. *Phys. Rev.* **1963**, *132*, 1507–1512.
- (38) Gerritsen, H. J.; Sabisky, E. S. Phys. Rev. 1962, 125, 1853–1859.

(39) Dodson, C. M.; Zia, R. Phys. Rev. B: Condens. Matter Mater. Phys. 2012, 86, 125102.

- (40) Rams, J.; Tejeda, A.; Cabrera, J. M. J. Appl. Phys. 1997, 82, 994-997.
- (41) Fromknecht, R.; Khubeis, I.; Meyer, O. Nucl. Instrum. Methods Phys. Res., Sect. B 1996, 116, 109-112.
- (42) Watkins, G. D. Phys. Rev. 1959, 113, 79-90.
- (43) Mims, W. B. Phys. Rev. 1968, 168, 370-389.
- (44) Cockroft, N. J.; Wright, J. C. Phys. Rev. B: Condens. Matter Mater. Phys. 1992, 45, 9642-9655.
- (45) Jiang, L.; Hodges, J. S.; Maze, J. R.; Maurer, P.; Taylor, J. M.; Cory, D. G.; Hemmer, P. R.; Walsworth, R. L.; Yacoby, A.; Zibrov, A. S.; Lukin, M. D. *Science* **2009**, *326*, *267*–*272*.
- (46) Ghoshtagore, R. N.; Noreika, A. J. J. Electrochem. Soc. 1970, 117, 1310-1314.